Journal of Electronic Research and Application, 2026, Volume 10, Issue 1
http://ojs.bbwpublisher.com/index.php/JERA
ISSN Online: 2208-3510
ISSN Print: 2208-3502

Design of Integrated Brushless Motor Drive and Control System for Robotic Arm Joints

Wei Liu, Tingyu Li

School of Information and Control Engineering, Jilin University of Chemical Technology, Jilin 132022, Jilin, China

**Author to whom correspondence should be addressed.*

Abstract: To meet the requirements of high performance, low cost, and modularity in robotic arm joints, this study designs an integrated brushless motor drive and control system. The system selects the STM32G473 microcontroller as the control chip and adopts field-oriented control as the primary motor control algorithm. Meanwhile, the drive and control system design is completed from both hardware and software aspects. Finally, the study performs closed-loop experiments on the robotic arm joint. The experimental results demonstrate that the designed drive and control system for robotic arm joints exhibits a favorable dynamic response and steady-state performance, making it suitable for controlling desktop-level and lightweight robotic arms.

Keywords: Robotic arm joint; Brushless motor; Motor drive; FOC

1. Introduction

Since the mid-20th century, with the rapid development of computer technology and automatic control, robotic arm technology has emerged and quickly become an important driving force for industrial automation and intelligence [1]. Over several decades of development, robotic arm technology has gradually matured, with research extending beyond traditional industrial manufacturing into emerging domains such as healthcare, service, and education. These new application scenarios impose higher demands on the lightweight design and flexibility of robotic arms [2]. In the control of a robotic arm, the joint motor, as the actuator driving the arm, has a direct impact on stability, dynamic performance, and execution accuracy [3]. However, traditional robotic joints often employ a separate drive-control design, which generally suffers from high costs and low integration. These drawbacks become increasingly pronounced in miniaturized and modular application scenarios [4]. Therefore, balancing performance, cost, and integration in joint drive and control systems has become a current research focus, and integrated drive and control design has emerged as a new development trend. In response to the above needs, this study designs an integrated drive and control system for robotic arm joints, conducting research from two aspects: hardware circuit design and motor control algorithm development. Experiments verify the system’s performance advantages in brushless motor control.

2. System hardware design

In terms of hardware selection, factors such as performance, cost, and integration are considered. The system hardware block diagram is shown in **Figure 1**.

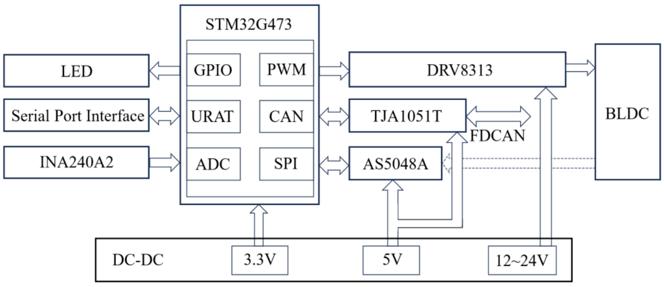

Figure 1. Hardware block diagram of the brushless motor drive and control system.

The main control chip selects the STM32G473 microcontroller as the computational core for the motor control algorithm. The drive section utilizes the DRV8313 three-phase brushless motor driver, and together with the AS5048A magnetic encoder and INA240A2 current-sensing chip, implements closed-loop motor control. Additionally, the drive and control board offers an FDCAN interface for data exchange with the host computer. The circuit design of each module is described in detail below.

2.1. Control module

The circuit design of the control module is shown in **Figure 2**, which comprises the MCU and its peripheral circuits. The motor drive control board selects the STM32G473 microcontroller as the control chip, featuring a single-precision FPU and a DSP instruction set, with a maximum frequency of 170 MHz. It is capable of handling the complex computations required by motor control algorithms. The MCU communicates with sensors, the driver module, and the host computer via SPI and FDCAN interfaces. Additionally, a UART serial port and an LED indicator are reserved to facilitate subsequent system development and debugging.

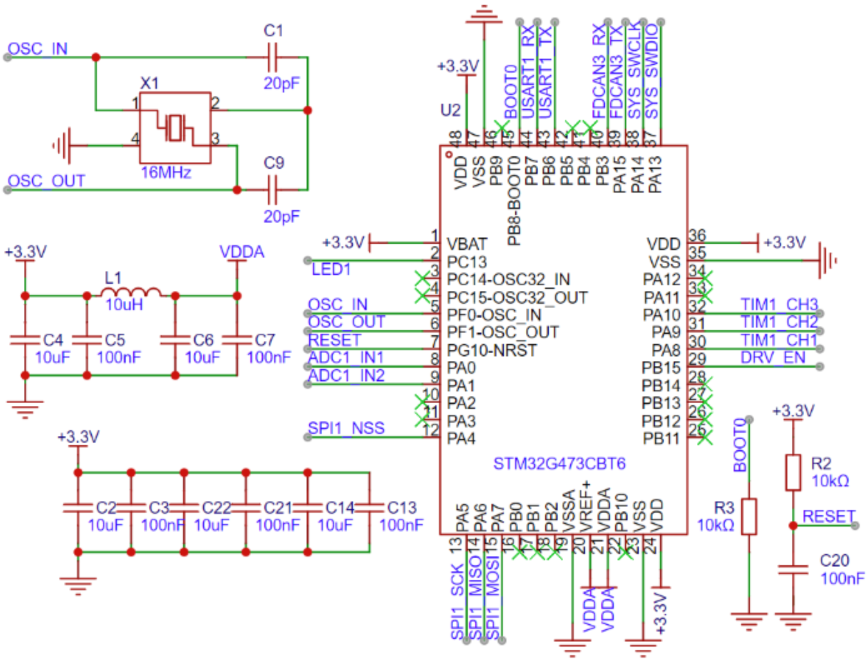

Figure 2. Control module circuit.

2.2. Motor drive module

The motor drive module employs the DRV8313 integrated driver chip, which internally integrates a complete pre-driver and three-phase half-bridge circuit. The input supply voltage ranges from 8V to 60V, and each half-bridge channel can deliver a peak current of up to 2.5A. The circuit of the drive module is shown in **Figure 3**. The STM32 controls the enable and conduction states of the three-phase drive through ENx and INx pins, respectively. The pre-driver amplifies these control signals to drive the power MOSFETs, which ultimately output to the three-phase windings via OUTx pins, achieving motor drive and control.

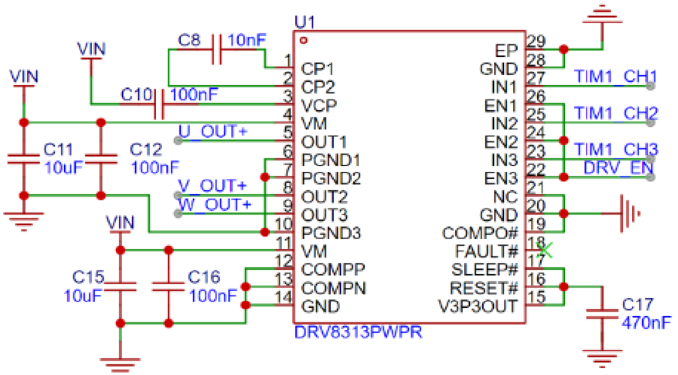

Figure 3. Motor drive module circuit.

2.3. Current sensing module

The circuit of the current sensing module is shown in **Figure 4**. The three-phase currents are measured using a combination of the dual-shunt resistor sampling method and the built-in current sensing function. The circuit directly connects the shunt resistors in series with the output terminals of motor phases U and V, amplifying the differential voltage across each resistor with a fixed gain of 50 V/V. The resulting output voltage signals are then fed into the ADC channels of the STM32.

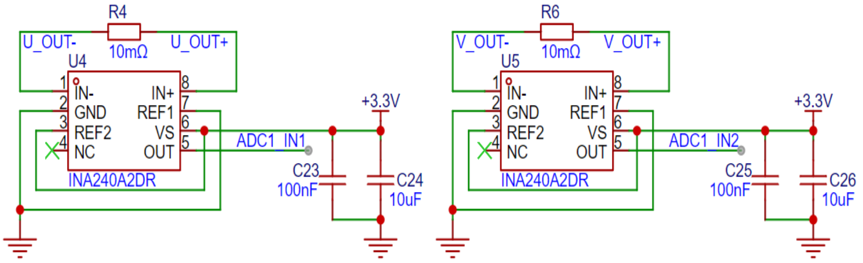

Figure 4. Current sensing module circuit.

2.4. Communication module

In this study, the robotic arm joint employs a distributed control architecture. Each joint controller exchanges high-frequency, bidirectional data with the host computer within a short time frame. Consequently, the communication scheme must ensure high speed, low latency, and strong reliability. To meet these requirements, the system uses the FDCAN protocol and employs the TJA1051T high-speed CAN transceiver, which supports data rates up to 5 Mbit/s to ensure reliable communication. The FDCAN communication module circuit is shown in **Figure 5**.

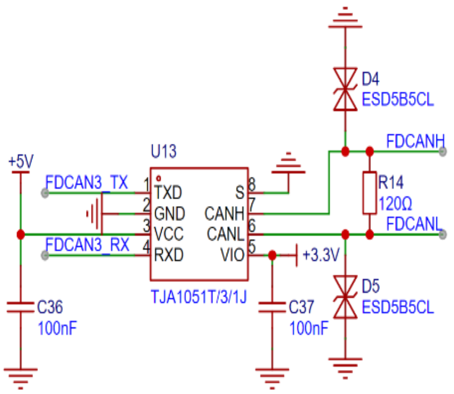

Figure 5. Communication module circuit.

2.5. Step-down module

The input voltage range of the motor drive and control board designed in this paper is 12V to 24V. To meet the power requirements of different modules, a multi-stage step-down scheme is adopted. As shown in **Figure 6**, the first-stage step-down circuit employs the synchronous step-down DC-DC converter SY8303AIC to convert 24 V to 5 V. The second-stage step-down then utilizes the linear LDO regulator RT9013-33GB to convert 5V to 3.3V.

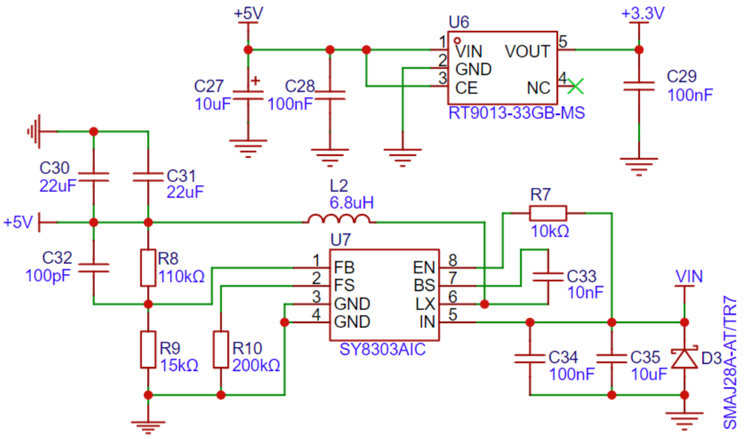

Figure 6. Step-down module circuit.

2.6. Magnetic encoder module

To improve the control accuracy and real-time performance of the robotic arm joints, the AS5048A magnetic rotary encoder is selected to acquire the motor angle information. This encoder features 14-bit high-resolution absolute angular measurement. The magnetic encoder module circuit is shown in **Figure 7**. Communication with the STM32 is achieved via the SPI interface, enabling high-speed data transmission and ensuring that joint angle information is fed back to the STM32 in real-time.

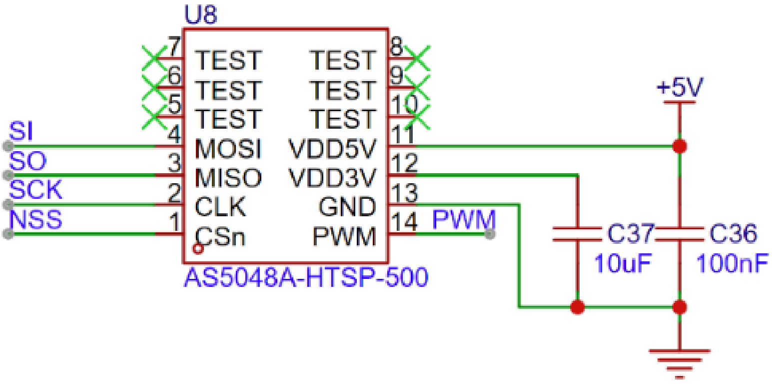

Figure 7. Magnetic encoder module circuit.

2.7. PCB design

The robotic arm joints employ an integrated design for the drive unit, which requires the integration of the reducer, motor, position sensor, and drive control board within the joint. Therefore, the designed PCB should be as compact as possible. Board size constraints make two-layer routing difficult, so the design adopts a four-layer PCB. The PCB design and physical layout are shown in **Figure 8** and **Figure 9**, with a board outline of 49 mm * 10 mm and all components placed on the top layer only. The top and bottom layers serve as signal routing layers, the GND layer forms a continuous ground plane, and the power layer carries only partial power traces.

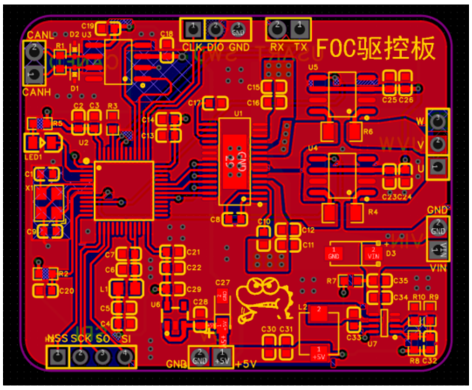

Figure 8. PCB layout of the board.

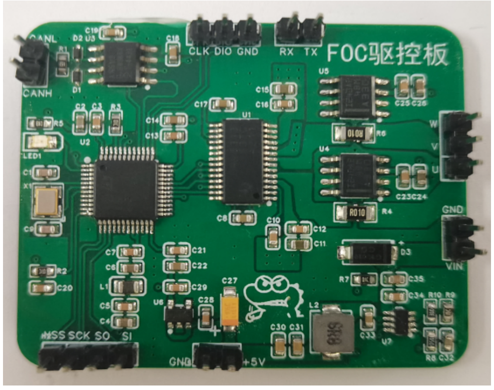

Figure 9. Physical board of the board.

3. Brushless motor FOC control

The Common control methods for BLDC motor include square wave control, sine control, and FOC control. In contrast, the first two methods suffer from limitations in terms of precision and stability. The FOC control can achieve high efficiency, smooth torque output, and high-precision position control over the full speed range, better meeting the stability and precision requirements of robotic arm joints. Therefore, this study adopts FOC as the core control algorithm for the BLDC motor.

FOC, also known as magnetic field-oriented control, is a type of vector control [5]. The basic framework of FOC control is shown in **Figure 10**. Its core idea is to decompose the stator current into a direct-axis component (I_d) controlling the field excitation and a quadrature-axis component (I_q) controlling the torque through a series of coordinate transformations, and regulating them independently to achieve high-precision control of the motor's magnetic field and torque. Meanwhile, three cascaded loops-position, speed, and current-are adopted, and the performance of each loop is optimized using PID control.

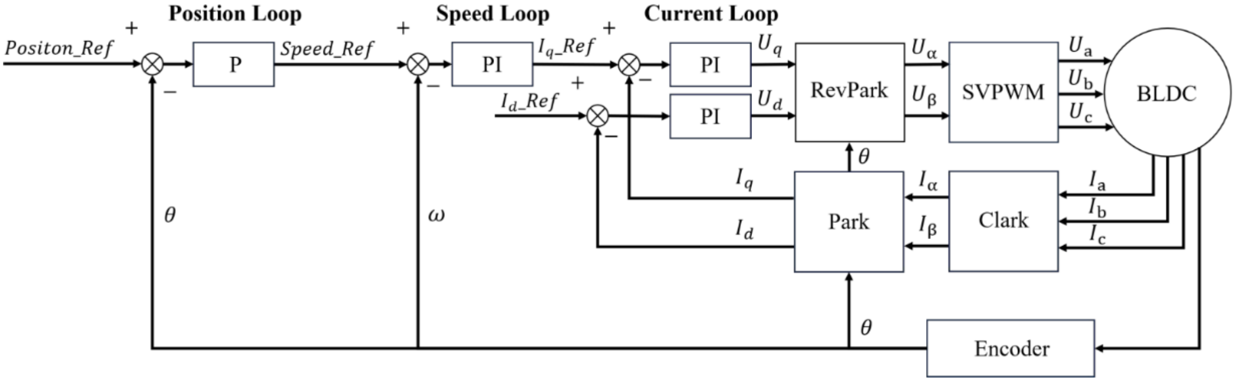

Figure 10. FOC three-loop control framework.

3.1. Clarke and Park transformation

The Clarke transformation is based on the principle of electromagnetic equivalence between the three-phase winding and two orthogonal windings [6]. It projects the current variables from the three-phase stationary reference frame onto a two-phase stationary orthogonal coordinate system. As shown in **Figure 11**, the current variables I_a, I_b, and I_c in the A-B-C coordinate system are projected on the α and β axes, to obtain the current components $I_α$ and $I_β$ in the two-phase stationary coordinate system.

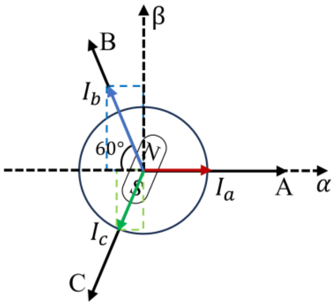

Figure 11. Clark transform.

Based on the coordinate relationships shown in **Figure 11**, the Clarke transformation can be expressed as follows:

$$\begin{cases} I_\alpha = I_a \\ I_\beta = \frac{1}{\sqrt{3}}(I_a + 2I_b) \end{cases} \tag{1}$$

After the Clarke transformation, the control variables are reduced from three to two, while the signal frequency remains unchanged before and after the transformation. However, the transformed variables I_α and I_β, remain sinusoidal and thus nonlinear.

Next, the Park transformation is applied to convert the two-phase stationary α-β coordinate system into the rotating d-q coordinate system, aligning with the rotor magnetic field. In this coordinate transformation, the d-axis is always aligned with the rotor flux direction, and the q-axis is orthogonal to the d-axis. This ensures that the current components maintain a fixed relationship with the magnetic field. As shown in **Figure 11**, the current components I_α and I_β in the α-β coordinate system are projected onto the d-q coordinate system.

Based on the coordinate relationships shown in **Figure 12**, the Park transformation can be expressed as follows:

$$\begin{cases} I_d = I_\alpha \cos\theta + I_\beta \sin\theta \\ I_q =- I_\alpha \sin\theta + I_\beta \cos\theta \end{cases} \tag{2}$$

Where θ is the rotor electrical angle. Through this transformation, the d-axis current I_d and q-axis current I_q in the rotating d-q coordinate system are obtained, thereby achieving decoupling and simplification of motor control.

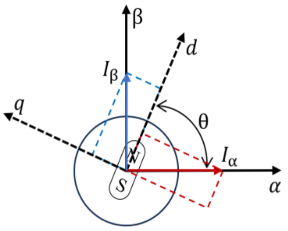

Figure 12. Park transform.

3.2. Space vector pulse width modulation

Through the inverse Park transformation, the AC reference voltage signals in the two-phase rotating d-q coordinate system, U_α and U_β, are obtained. These signals then need to be converted into three-phase voltages U_a, U_b, and U_c to drive the three-phase inverter circuit. Therefore, Space Vector Pulse Width Modulation (SVPWM) is employed to generate six high-frequency PWM signals. By controlling the on/off sequence of the six power MOSFETs, the desired three-phase sinusoidal AC voltages are produced [7].

In a three-phase inverter circuit, let the conduction of the upper switch in a half-bridge $Sx(x= a, b, c)$ correspond to state 1, and the conduction of the lower switch correspond to state 0. The upper and lower switches of the same half-bridge cannot conduct simultaneously. Based on this definition, the combination of the three-phase switch states can generate eight distinct basic voltage space vector states: U_{100}, U_{110}, U_{010}, U_{011}, U_{001}, U_{101}, U_{111}, U_{000}.

Taking one of the non-zero voltage vectors U_{100} for analysis, when the upper switch of phase A and the lower switches of phases B and C are conducting. Assuming equal phase resistances and a DC bus voltage of U_{dc}, the phase voltages U_{aN}, U_{bN} and U_{cN} relative to the neutral point N are as follows: $2/3U_{dc}$, $-1/3U_{dc}$ and $-1/3U_{dc}$. The synthesized expression of the three-phase symmetrical sinusoidal voltage vector is given in **Equation (3)**:

$$\vec{U}_{out} = \frac{2}{3}\left(U_{aN} + U_{bN}e^{j\frac{2\pi}{3}} + U_{cN}e^{j\frac{4\pi}{3}}\right) \tag{3}$$

After substituting U_{aN}, U_{bN} and U_{cN} into Equation (3), the resultant vector U_{100} can be obtained as:

$$U_{100} = \frac{2}{3}\left[\frac{2}{3}U_{\mathrm{dc}} - \frac{1}{3}U_{\mathrm{dc}}\left(cos\frac{2\pi}{3} + jsin\frac{2\pi}{3}\right) - \frac{1}{3}U_{\mathrm{dc}}\left(cos\frac{2\pi}{3} - jsin\frac{2\pi}{3}\right)\right] = \frac{2}{3}U_{\mathrm{dc}} \tag{4}$$

Similarly, the remaining non-zero voltage vectors can be calculated. In the α-β coordinate system, the six non-zero vectors have equal magnitudes of $2/3U_{dc}$, and each adjacent non-zero vector is separated by 60°. The two zero vectors have zero magnitude and are located at the center. The endpoints of the six non-zero basic voltage vectors form a regular hexagon, dividing the plane into six sectors, as shown in **Figure 13**.

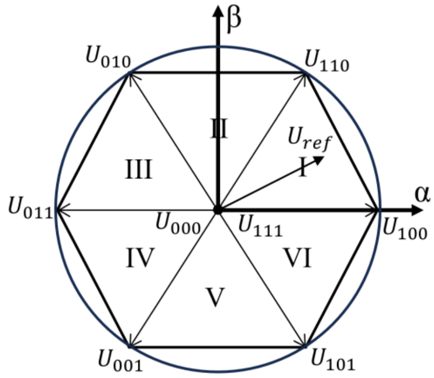

Figure 13. Voltage space vector diagram.

According to the principle of volt-second balance, any desired voltage vector U_{ref} in the α-β coordinate system, composed of U_α and U_β, can be synthesized by controlling the duration of the two adjacent non-zero basic vectors within the sector and the zero vectors. Let a PWM period be T_s, and the desired reference vector during this period be U_{ref}. Denote the two adjacent non-zero basic vectors of the sector as U_x and U_y, and the zero vector as U_0. Then, according to the volt-second balance principle, the **Equation (5)** can be derived:

$$U_{\mathrm{ref}} \cdot T_s = \overrightarrow{U_x} \cdot T_x + \overrightarrow{U_y} \cdot T_y + \overrightarrow{U_0} \cdot T_0 \tag{5}$$

In summary, the SVPWM technique synthesizes a reference voltage vector U_{ref} from U_α and U_β obtained via the inverse Park transformation. The sector in which the reference vector is located is then determined. The dwell times of the two adjacent active vectors within the sector, along with the zero vectors, are appropriately allocated. Once the required dwell times of the adjacent active vectors and zero vectors are calculated, the PWM signals are generated. These PWM signals drive the three-phase inverter, ultimately achieving precise control of the brushless motor.

4. Results and discussion

To evaluate the performance of the BLDC motor drive and control system designed in this study, a position closed-loop test was conducted. This test also aimed to verify the FOC algorithm and assess the stability, accuracy, and real-time performance of the control system. The initial position was set to 0°. The motor was commanded to move to target positions of 90°, 180°, and 360°. Real-time data were recorded and analyzed using MATLAB.

As shown in **Figure 14** and **Figure 15**, when the motor moved from 0° to 90°, the system response time was 0.138s. The settling time was approximately 0.498s. After stabilization, the maximum error was about 0.25°. The average error remained within 0.2°.

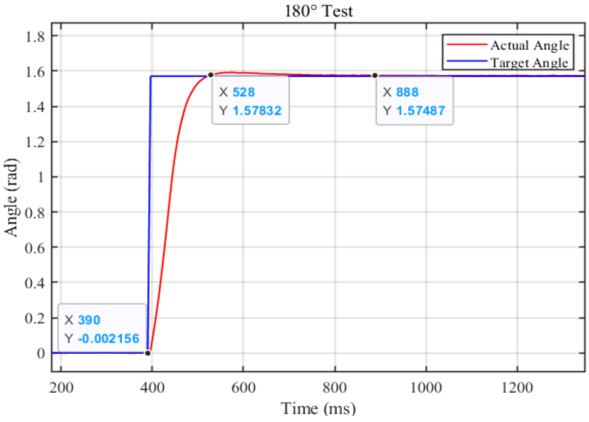

Figure 14. Response curve at 90° position.

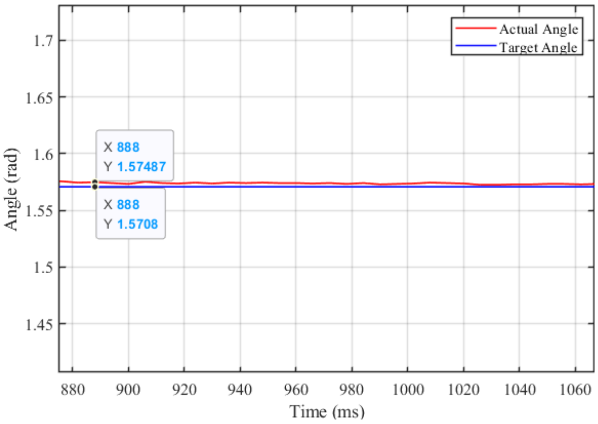

Figure 15. Position error curve at 90°

As shown in **Figure 16** and **Figure 17**, when the motor moved from 0° to 180°, the system response time is approximately 0.216s, the settling time is about 0.372s, the maximum steady-state error is around 0.18°, and the average error does not exceed 0.13°.

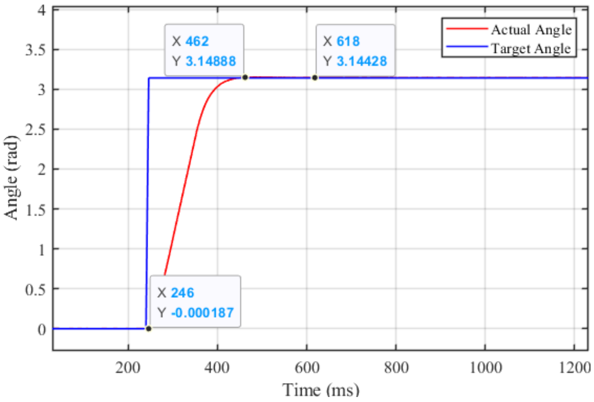

Figure 16. Response curve at 180° position.

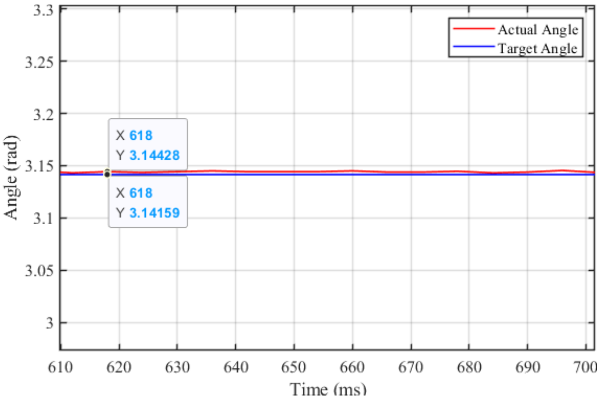

Figure 17. Position error curve at 180°.

As shown in **Figure 18** and **Figure 19**, when the motor moved from 0° to 360°, the system response time is approximately 0.378s. The maximum steady-state error is about 0.15°, and the average steady-state error is controlled within 0.12°.

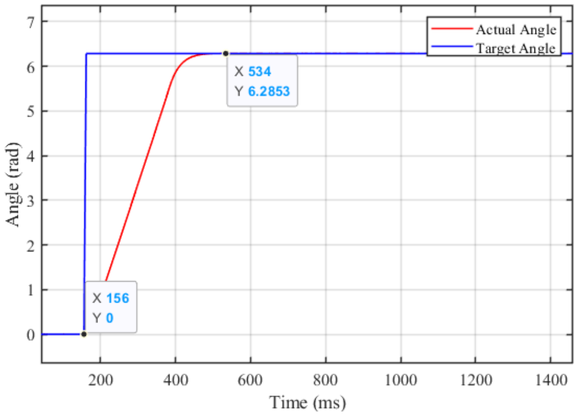

Figure 18. Response curve at 360° position.

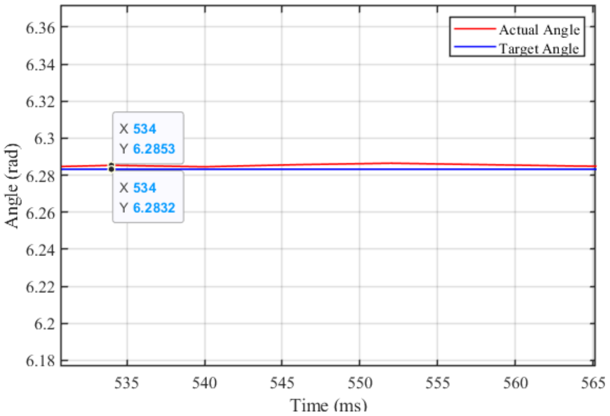

Figure 19. Position error curve at 360°.

The above experiments indicate that the system demonstrates superior dynamic response, with minimal steady-state position error. The maximum steady-state error does not exceed 0.25°, and the average steady-state error remains within 0.2°.

5. Conclusion

This study designs an integrated BLDC motor drive and control system for robotic arm joints, featuring high performance, high integration, and low cost. Experimental results show that the designed system exhibits excellent dynamic response and steady-state performance, meeting the requirements of desktop, lightweight robotic arms.

Disclosure statement

The author declares no conflict of interest.

References

[1] Ye S, Sun L, 2021, Design and Implementation of Intelligent Control Program for Six Axis Joint Robot. Big Data Analytics for Cyber-Physical System in Smart City, 180–186.

[2] Sathuluri A, Sureshbabu A, Frank J, et al., 2023, Computational Systems Design of Low-Cost Lightweight Robots. Robotics, 12(4): 91.

[3] Tingting W, 2023, Research on Optimized Control Method for Robotic Arm Joint Motors, thesis, Changchun University of Technology.

[4] Le Q, 2024, Neural Network FOC Control of Robotic Arms Driven by Brushless Motors, thesis, Xi’an Shiyou University.

[5] Li N, Li M, Zhang C, et al., 2024, Design of Brushless Motor Control System Based on FOC Algorithm. International Conference on Mechatronic Engineering and Artificial Intelligence, 130712T.1–130712T.7.

[6] O’Rourke C, Qasim M, Overlin M, et al., 2019, A Geometric Interpretation of Reference Frames and Transformations: dq0, Clarke, and Park. IEEE Transactions on Energy Conversion, 34(4): 2070–2083.

[7] Ma R, Guo X, Zhang Y, et al., 2023, PMSG Offshore Wind Power System Control Using SMC and ADRC with Fast SVPWM in Complicated Environment. Electrical Engineering, 105(5): 2751–2767.